Effects of Ocean Slow Response under Low Warming Targets

SHANG-MIN LONG,[a,b,c] SHANG-PING XIE,[d] YAN DU,[c,e,f] QINYU LIU,[g] XIAO-TONG ZHENG,[g,h,i] GANG HUANG,[j] KAI-MING HU,[j] AND JUN YING[b]

[a] *International Polar Environment Research Laboratory, College of Oceanography, Hohai University, Nanjing, China*
[b] *State Key Laboratory of Satellite Ocean Environment Dynamics, Ministry of Natural Resources, Hangzhou, China*
[c] *State Key Laboratory of Tropical Oceanography, South China Sea Institute of Oceanology, Chinese Academy of Sciences, Guangzhou, China*
[d] *Scripps Institution of Oceanography, University of California, San Diego, La Jolla, California*
[e] *University of Chinese Academy of Sciences, Beijing, China*
[f] *Southern Marine Science and Engineering Guangdong Laboratory, Guangzhou, China*
[g] *Physical Oceanography Laboratory, Collaborative Innovation Center of Marine Science and Technology, Ocean University of China, Qingdao, China*
[h] *Qingdao National Laboratory for Marine Science and Technology, Qingdao, China*
[i] *College of Oceanic and Atmospheric Sciences, Ocean University of China, Qingdao, China*
[j] *State Key Laboratory of Numerical Modeling for Atmospheric Sciences and Geophysical Fluid Dynamics and Center for Monsoon System Research, Institute of Atmospheric Physics, Chinese Academy of Sciences, Beijing, China*

(Manuscript received 18 March 2019, in final form 1 October 2019)

ABSTRACT

The 2015 Paris Agreement proposed targets to limit global-mean surface temperature (GMST) rise well below 2°C relative to preindustrial level by 2100, requiring a cease in the radiative forcing (RF) increase in the near future. In response to changing RF, the deep ocean responds slowly (ocean slow response), in contrast to the fast ocean mixed layer adjustment. The role of the ocean slow response under low warming targets is investigated using representative concentration pathway (RCP) 2.6 simulations from phase 5 of the Coupled Model Intercomparison Project. In RCP2.6, the deep ocean continues to warm while RF decreases after reaching a peak. The deep ocean warming helps to shape the trajectories of GMST and fuels persistent thermosteric sea level rise. A diagnostic method is used to decompose further changes after the RF peak into a slow warming component under constant peak RF and a cooling component due to the decreasing RF. Specifically, the slow warming component amounts to 0.2°C (0.6°C) by 2100 (2300), raising the hurdle for achieving the low warming targets. When RF declines, the deep ocean warming takes place in all basins but is the most pronounced in the Southern Ocean and Atlantic Ocean where surface heat uptake is the largest. The climatology and change of meridional overturning circulation are both important for the deep ocean warming. To keep the GMST rise at a low level, substantial decrease in RF is required to offset the warming effect from the ocean slow response.

1. Introduction

Recent studies reveal that global-mean surface temperature (GMST) has risen more than 1°C relative to preindustrial level (Blunden and Arndt 2017; Xie and Kosaka 2017), causing significant climate impacts (Church and White 2011; Blunden and Arndt 2017; Cheng et al. 2019). Additional increase in GMST would intensify the risk of sea level rise, increase extreme event occurrences, and cause irreversible damages on ecosystem (Schaeffer et al. 2012; Schleussner et al. 2017; Li et al. 2018). To avoid dangerous climate change, the 2°C warming level is suggested as the threshold for GMST rise (Mann 2009). The 2015 Paris Agreement further proposed a more ambitious target of keeping GMST rise well below 2°C and as low as 1.5°C by 2100 relative to preindustrial level. These warming goals are much lower than projections from climate models under emission scenarios with moderate or no mitigation efforts (van Vuuren et al. 2011; IPCC 2013).

The low warming targets generate heated debates on carbon emissions control policy, possible emission

Supplemental information related to this paper is available at the Journals Online website: https://doi.org/10.1175/JCLI-D-19-0213.s1.

Corresponding author: Yan Du, duyan@scsio.ac.cn

DOI: 10.1175/JCLI-D-19-0213.1

pathways to achieve them (Sanderson et al. 2016; Xu and Ramanathan 2017), and the climate impacts under such conditions (Li et al. 2018; Palter et al. 2018; IPCC 2018). Previous studies show that to achieve the 2° or 1.5°C warming level, a steep reduction in carbon emissions needs to be implemented as soon as possible. To fully achieve that goal, zero or even negative carbon emissions are required, which may result in a decrease in atmospheric greenhouse gas (GHG) concentrations and hence radiative forcing (RF) in the near future (Rogelj et al. 2013; Sanderson et al. 2017). Given the importance of ocean in mediating regional climate change under global warming (Manabe and Stouffer 2007; Rhein et al. 2013; Xie et al. 2015), it is natural to ask how climate will respond under such low warming targets and what is the role of ocean response in shaping future climate changes, especially when RF gradually decreases.

In response to changing RF, the ocean mixed layer adjusts quickly (ocean fast response) but the deep ocean responds slowly (ocean slow response) due to its huge heat capacity and the slow ocean circulation and mixing (Held et al. 2010). The ocean fast response dominates GMST change when RF increases, but the percentage contribution from ocean slow response is expected to increase when the increase in RF ceases based on a one-dimensional two-box model (Long et al. 2018). The effect of the deep ocean slow warming on GMST and global-mean sea level persists for centuries after the cease of anthropogenic carbon emissions (Frölicher et al. 2014; Zickfeld et al. 2017). While the importance of ocean slow response is suggested previously (Manabe et al. 1990; Held et al. 2010; Chadwick et al. 2013; Long et al. 2014), its effect on global and regional climate when the increase in RF is ceased has not been systematically studied.

Representative concentration pathways (RCPs) 2.6 and 4.5 both feature an end in RF increase before 2100. Using simulations from phase 5 of the Coupled Model Intercomparison Project (CMIP5) (Taylor et al. 2012), the present study investigates the role of ocean slow response in changes under decreased RF in RCP2.6 that is in line with the low warming targets. We show that in RCP2.6, the persistent deep ocean warming with decreasing RF mainly results from ocean slow response with constant peak RF. This deep layer warming is a robust feature across basins that would strongly influence surface climate system. The slow warming component resulting from the ocean slow response contributes in important ways to global and regional changes in surface temperature, sea level, and ocean heat content (OHC) after the RF peak in RCP2.6. It also contributes a sizeable GMST rise, which is important for achieving the low warming targets. Ocean dynamics causes substantial regional difference in the penetration depth of ocean warming. Indeed, the deep ocean warming is the most prominent in the Southern Ocean and North Atlantic, a result of the active ocean heat uptake (OHU) and significant heat redistribution. Furthermore, the atmosphere persistently warms the Southern Ocean and North Atlantic despite the RF decrease, mainly because the air–sea warming contrasts remain positive there through 2300. We further explore the processes associated with the meridional overturning circulation (MOC) that are for the deep ocean warming.

The rest of the paper is organized as follows. Section 2 describes the methods and data from CMIP5 models. Section 3 shows global-mean responses in RCP2.6 and contributions from different components. Section 4 investigates patterns of surface warming and OHC change in RCP2.6. Section 5 discusses oceanic processes associated with the deep ocean warming. Section 6 is a summary with discussion.

2. Data and methods

a. Data

Monthly outputs of historical (1850–2005), RCP2.6 (2006–2100), and RCP4.5 (2006–2100) runs from 24 CMIP5 models are analyzed. Among the 24 models, extended simulations to 2299 or 2300 are available in 9 (14) models in RCP2.6 (RCP4.5) (Table 1). Particularly, eight models have the extension runs from both RCP2.6 and RCP4.5. This facilitates the multimodel analyses of long-term ocean slow response and its effect on the climate system. Near-surface (nominally at 2 m) air temperature (tas), surface temperature (ts; also called ''skin'' temperature, i.e., SST for open ocean), precipitation (pr), surface wind stress (tauu and tauv), seawater potential temperature (PT), seawater potential density (PD), and seawater velocity (vo) are used in this study. All atmospheric and oceanic variables are respectively interpolated onto common grids of 2.5° latitude × 2.5° longitude and 1° latitude × 1° longitude for easy comparison. The first member (r1i1p1) of each model is analyzed.

The Eulerian-mean meridional overturning circulation (MOC) is estimated by calculating the meridional overturning streamfunction based on monthly meridional velocity field (Liu et al. 2018). The Atlantic MOC (AMOC) index is defined as the maximum value of MOC at 40°N. OHU is measured by time-integrated surface heat flux into ocean referenced to preindustrial (1850–99) level, while OHC is calculated by vertically integrating the ocean temperature. Ocean heat storage (OHS) of a specific region refers to the area-weighted vertically integrated OHC.

TABLE 1. Names and expansions of 24 CMIP5 coupled models used in this study. The last year (2299 or 2300) of the models with RCP extensions is listed.

Model name	Expansion	RCP2.6	RCP4.5
BCC-CSM1.1	Beijing Climate Center (BCC), Climate System Model (CSM), version 1.1	**2300**	**2300**
BCC-CSM1.1 (m)	BCC-CSM1.1, medium resolution		
BNU-ESM	Beijing Normal University–Earth System Model		
CanESM2	Second Generation Canadian Earth System Model	**2300**	**2300**
CCSM4	Community Climate System Model (CCSM), version 4	**2300**	**2300**
CESM1-CAM5	CESM1 using Community Atmosphere Model, version 5	**2300**	**2300**
CNRM-CM5	Centre National de Recherches Météorologiques Coupled Global Climate Model, version 5		**2300**
CSIRO-Mk3.6.0	Commonwealth Scientific and Industrial Research Organization (CSIRO), Mk3.0 Model		**2300**
GFDL CM3	Geophysical Fluid Dynamics Laboratory Climate Model (GFDL), version 3		**2300**
GFDL-ESM2G	GFDL Earth System Model with Generalized Ocean Layer Dynamics component		
GFDL-ESM2M	GFDL Earth System Model with Modular Ocean Model, version 4 component		
GISS-E2-R	NASA Goddard Institute for Space Studies, ModelE	**2300**	**2300**
HadGEM2-AO	Hadley Centre Global Environment Model, version 2 Atmosphere–Ocean		
HadGEM2-ES	Hadley Centre Global Environment Model, version 2–Earth System	**2299**	**2299**
IPSL-CM5A-LR	L'Institut Pierre-Simon Laplace (IPSL) Coupled Model, version 5A, coupled with NEMO, low resolution	**2300**	**2300**
IPSL-CM5A-MR	IPSL Coupled Model, version 5A, coupled with NEMO, mid resolution		**2300**
MIROC-ESM	Model for Interdisciplinary Research on Climate (MIROC), Earth System Model (ESM)		**2300**
MIROC-ESM-CHEM	MIROC-ESM Chemistry Coupled Model		
MIROC5	MIROC, version 5	**2300**	
MPI-ESM-LR	Max Planck Institute Earth System Model (MPI-ESM), low resolution	**2300**	**2300**
MPI-ESM-MR	MPI-ESM, medium resolution		
MRI-CGCM3	Meteorological Research Institute Coupled Atmosphere–Ocean General Circulation Model, version 3		
NorESM1-M	Norwegian Climate Centre Earth System Model, version 1 (medium resolution)		**2300**
NorESM1-ME	Norwegian Climate Centre Earth System Model, version 1E (medium resolution with capability to be fully emission driven)		

In RCP2.6, RF reaches a peak of 3.0 W m^{-2} around 2045 and then decreases to 2.6 W m^{-2} at 2100 and 1.6 W m^{-2} by 2300 (Taylor et al. 2012). In RCP4.5, RF increases quickly to a value very close to 4.5 W m^{-2} around 2070 and then holds constant. As discussed in a previous study (Long et al. 2014), further changes after the RF stabilization are due to ocean slow response. In this study, the year when RF transitions from increase to decrease or stabilization is called "the RF inflection point," while change after the RF peak in RCP2.6 is called "post-RF peak change."

We first estimate the temperature change ΔT around the RF inflection point as the differences between time means of 2040–60 (2060–80) and 1850–99 in RCP2.6 (RCP4.5). The center of the period (2050) in RCP2.6 is chosen to lead the RF inflection point (2045) by 5 years because the time scale for the ocean fast response is

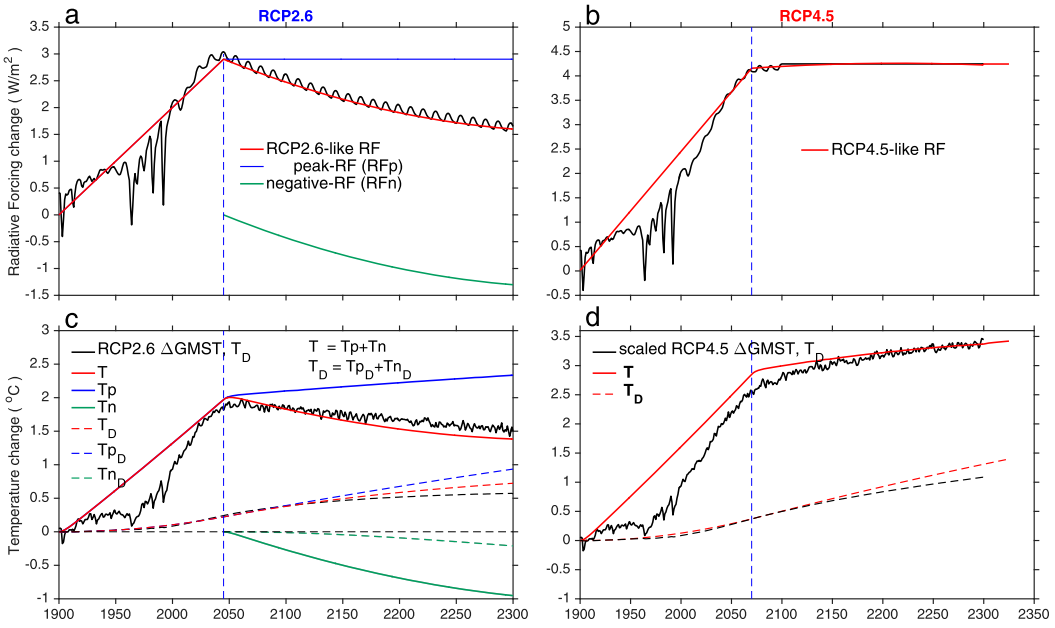

FIG. 1. RF in RCP2.6 and RCP4.5 (black lines) and in idealized scenarios: (a) RCP2.6-like scenario (red line), constant peak-RF scenario (RFp; blue line), and negative RF scenario (RFn; green line); and (b) RCP4.5-like scenario. GMST change (black line) and 0–3000-m ocean temperature change (black dashed line) in (c) RCP2.6 and (d) RCP4.5 and global-mean surface temperature (solid color lines) and deep ocean temperature change (dashed color lines) in idealized scenarios.

3–5 years (Held et al. 2010). In RCP4.5, RF displays rather small variations in the 5 years before 2070, so we just center the period in RCP4.5 at 2070. The further changes after the RF inflection denoted by a prime $\Delta T'$, are calculated by the 21-yr mean at the end of each century (2080–2100, 2180–2200, 2280–2300) minus the 2040–60 (2060–80) mean in RCP2.6 (RCP4.5).

b. *The two-box model*

Global-mean surface temperature change can be understood based on a simple two-box model for the ocean mixed layer and deep ocean (Gregory 2000; Held et al. 2010):

$$c_m \frac{\partial T}{\partial t} = Q - \varepsilon_a T - \varepsilon_o (T - T_D), \tag{1}$$

$$c_d \frac{\partial T_D}{\partial t} = \varepsilon_o (T - T_D). \tag{2}$$

Here, T is the global-mean surface temperature change, T_D is deep ocean temperature change, Q is the external radiative forcing, ε_a is the radiative damping rate, and ε_o is the mixing coefficient between the ocean mixed layer and deep ocean; also, $c_m = 6.17\,\mathrm{W\,yr\,m^{-2}\,K^{-1}}$and $c_d = 370.05\,\mathrm{W\,yr\,m^{-2}\,K^{-1}}$ are the heat capacity of an ocean mixed layer and a deep ocean with depths of 50 m and 3000 m, respectively. We set $\varepsilon_a = 0.85\,\mathrm{W\,m^{-2}\,K^{-1}}$ and $\varepsilon_o = 0.65\,\mathrm{W\,m^{-2}\,K^{-1}}$ to keep the two-box model-simulated GMST change (red lines in Figs. 1c,d) under idealized RCP2.6-like and RCP4.5-like scenarios (red lines in Figs. 1a,b) close to that in CMIP5 models (black lines in Figs. 1c,d). Discrepancies between the CMIP5 model results and the two-box model may mainly due to the time dependence of ε_a and ε_o (Williams et al. 2008; Held et al. 2010; Winton et al. 2010; Geoffroy et al. 2013a,b). Here we utilize this simple two-box model and idealized scenarios to gain conceptual understanding rather than to conduct a quantitative analysis of the two-box model's behavior as in Geoffroy et al. (2013a,b).

For slowly varying RF, the ocean mixed layer is in quasi-equilibrium [the left-hand side of Eq. (1) is negligible] (Held et al. 2010; Long et al. 2014):

$$0 = Q - \varepsilon_a T - \varepsilon_o (T - T_D). \tag{3}$$

In a low warming scenario like RCP2.6 (Fig. 1a), when RF increases, T_D is relatively small at the early stage (Fig. 1c, red dashed line), and the first-order approximation of Eq. (3) is

$$T_0 = \frac{Q(t)}{\varepsilon_a + \varepsilon_o}. \tag{4}$$

It is a result of the ocean mixed layer fast adjustment under external RF, defined as ocean fast response

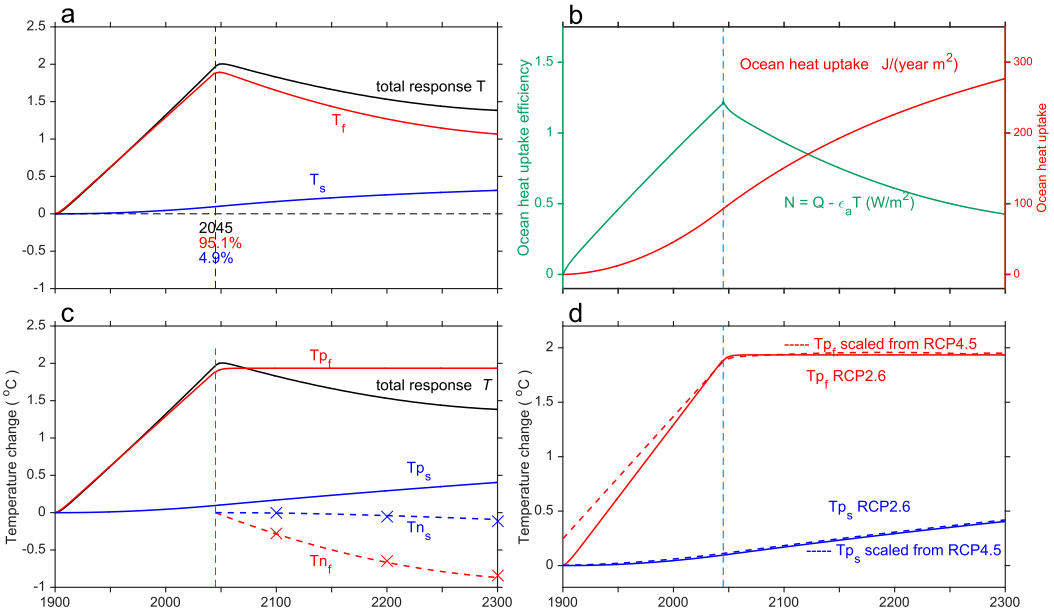

FIG. 2. Diagrams for (a) time-varying GMST change and its subcomponents from ocean fast (red line) and slow responses (blue line) under the low warming scenario where RF (dashed light blue line) first increases and then decreases, and (b) surface heat absorbed by ocean $\{N = Q - \varepsilon_a T = [\varepsilon_o/(\varepsilon_a + \varepsilon_o)](Q - \varepsilon_a T_D)$; blue line} and ocean heat uptake (OHU = $\int_0^t N\,dt$; red line). (c) Subcomponents of further change in T, with Tp_f and Tp_s (red lines), respectively, for fast and slow components under the constant peak RF scenario (RFp) and Tn_f and Tn_s for fast and slow components under negative RF scenario (RFn). (d) Tp_f and Tp_s in RFp scenario and the results scaled by GMST ratio from RCP4.5-like scenario. Because there is a time lag in the RF inflection point between RFp and RCP4.5-like scenarios, we shift the scaled time series (dashed lines) backward to fix the inflection points of the two scenarios at the same location for better comparison.

$[T_f \equiv Q(t)/(\varepsilon_a + \varepsilon_o)]$. As the deep ocean gradually warms, especially when RF decreases, T_D is not negligible, and the correction to T from the deep ocean warming is

$$T_1 = \frac{\varepsilon_o T_D(t)}{\varepsilon_a + \varepsilon_o}. \tag{5}$$

We define it as ocean slow response $[T_s \equiv \varepsilon_o T_D(t)/(\varepsilon_a + \varepsilon_o)$; blue line in Fig. 2a]. The full response of T can thus be written as

$$T = \frac{Q(t)}{\varepsilon_a + \varepsilon_o} + \frac{\varepsilon_o T_D(t)}{\varepsilon_a + \varepsilon_o}. \tag{6}$$

It is the sum of the fast and slow components at any given time t. Specifically, the heat absorbed by the ocean is the TOA RF minus the heat emitted by the warming atmosphere ($N = Q - \varepsilon_a T$; blue line in Fig. 2d). Therefore, N is positive before the full equilibrium state ($T = T_D = Q/\varepsilon_a$) of the two-box model is achieved. The accumulated ocean heat uptake is the time integral of the net surface heat into the ocean $(\mathrm{OHU} = \int_0^t N dt)$. As a result, despite RF decreases after the peak, OHU continually increases because the full equilibrium has not reached by 2300 (red and green line in Fig. 2b).

c. *Diagnostic method to separate the warming and cooling components in RCP2.6*

To understand the response in RCP2.6, we can estimate the further change in T (denoted as T') after the RF peak time t_p as

$$T' = \frac{Q'(t)}{\varepsilon_a + \varepsilon_o} + \frac{\varepsilon_o T_D'(t)}{\varepsilon_a + \varepsilon_o}. \tag{7}$$

Here $T' = T(t) - T(t_p)$, $Q' = Q(t) - Q(t_p)$. It can be viewed as the combination of the results under two scenarios: one with constant peak RF (denoted as RFp; blue line in Fig. 1a), and one forced by negative RF, that is, deviation from the peak RF (denoted as RFn; green line in Fig. 1a). The results under these two scenarios (blue and green lines in Fig. 1c) can be linearly added to well reproduce the total response (red line in Fig. 1c). The reason to do such scenario decomposition is because the RFp scenario displays the effect of peak RF, which relates to the largest amount of accumulated anthropogenic GHG concentration, while the RFn scenario gives us information about the consequences of

negative carbon emission action. Furthermore, the RFp scenario is similar to the RCP4.5 scenario in CMIP5, and we can understand climate response under low warming scenario like RCP2.6 by comparing with the results from RCP4.5.

Given that the change of the fast component under constant RF (Tp_f) is zero (Fig. 2c), Eq. (7) can be further written as

$$T' = \frac{Q'(t)}{\varepsilon_a + \varepsilon_o} + \frac{\varepsilon_o \mathrm{Tn}_D(t)}{\varepsilon_a + \varepsilon_o} + \frac{\varepsilon_o \mathrm{Tp}_D(t)}{\varepsilon_a + \varepsilon_o}. \tag{8}$$

Here Tn_D and Tp_D respectively denote deep ocean temperature change under RFn and RFp scenario and $T'_D = \mathrm{Tn}_D + \mathrm{Tp}_D$ (Fig. 1c). The first and second terms on the right-hand side of the equation are, respectively, the fast and slow component in response to the negative RF [$\mathrm{Tn}_f = Q'(t)/(\varepsilon_a + \varepsilon_o)$, $\mathrm{Tn}_s = \varepsilon_o \mathrm{Tn}_D(t)/(\varepsilon_a + \varepsilon_o)$], and the third term is the slow component forced by constant peak RF [$\mathrm{Tp}_s = \varepsilon_o \mathrm{Tp}_D(t)/(\varepsilon_a + \varepsilon_o)$]. For $t > t_p$, Tn_f and Tn_s decrease surface temperature (denoted as the cooling component) while Tp_s increases surface temperature (denoted as the slow warming component). Post-RF peak change T' can be deemed as a sum of the cooling component due to negative RF and the warming component due to ocean slow response with constant peak RF.

The RFp scenario is similar to the RCP4.5 scenario, indicating that we can separate the cooling and warming components of the post-RF peak change in RCP2.6 by utilizing results from RCP4.5. When RF increases, T_D falls far behind T (Fig. 1c) and Eqs. (2) and (6) can be respectively approximated as $\partial T_D/\partial t \approx \varepsilon_o T$ and $T \approx Q(t)/(\varepsilon_a + \varepsilon_o)$. At the RF inflection point, the magnitudes of T_f, T, and T_D are all nearly linear to T, which further determines the magnitude of ocean slow response with constant RF. Therefore, we can scale results in RCP4.5 scenario by GMST change at the RF inflection point to infer the slow warming component in RCP2.6. Indeed, when scaled by the ratio between $T(t_p)$ in two scenarios, results from RCP4.5-like scenario after the RF inflection point (Fig. 2d, dashed lines) compare well with those directly from RFp scenario (Fig. 2d, solid lines), confirming the validity of this decomposition method.

Based on the above discussion, we estimate the post-RF peak warming component in RCP2.6 by scaling $\Delta T'$ in RCP4.5 with the ratio of the GMST rise at the RF inflection point in RCP2.6 (1.87°C) to that in RCP4.5 (2.54°C). In RCP2.6, the difference between $\Delta T'$ and the warming component estimated above is the post-RF peak cooling component. Furthermore, the fast cooling component under the negative RF (Tn_f; red cross in Fig. 2c) can be estimated by scaling $T_f(t_p)$ with the ratio between Q' and $Q(t_p)$. In RCP2.6, $T_f(t_p)$ is well approximated by $T(t_p)$ because the former accounts for 95% of the latter (percentage labeled in Fig. 2a). The difference between the post-RF peak total cooling component and the RF-scaled fast cooling component is thus estimated as slow cooling component (Tn_s). Indeed, the scaled results are highly consistent with the two-box model results (crosses and dashed lines in Fig. 2c).

It is worth noting that when RF decreases, the fast cooling response to the negative RF dominates the slow cooling response ($\mathrm{Tn}_f \gg \mathrm{Tn}_s$; Fig. 2c), the same as the case during the RF increase period (Fig. 2a). Because the increase in RF starts much earlier and is much larger in magnitude than the decrease in RF, the post-RF peak slow cooling component is also much smaller than the slow warming component, reaching only 1/4 at the end of the twenty-third century.

3. Global-mean effects of ocean slow response

Figure 3 displays the time evolution of global-mean ocean potential temperature change (ΔPT) through 2300 from the eight-model ensemble-mean in RCP2.6 (left) and RCP4.5 (right). Differences in warming structures between RCP2.6 and RCP4.5 indicate the effect of the negative RF in the postpeak RF period, while their similarities suggest the role of the ocean slow response with constant peak RF. When RF increases, the upper ocean (0–100 m) warms much faster than the deep ocean (Figs. 3a,b), resulting in a sharp increase in vertical temperature stratification. After the RF inflection point (white dashed lines), the upper ocean temperature warming gradually weakens in RCP2.6 (Fig. 3a), whereas it continues after 2100 in RCP4.5 (Fig. 3b). This difference between RCP2.6 and RCP4.5 is more evident in changes following the RF inflection point (ΔPT′; Figs. 3c,d), with the upper ocean cooling in RCP2.6 but still warming in RCP4.5. The enhanced and continual warming in the deep layer is robust in both scenarios, especially after 2100, suggesting that the persistent deep ocean warming in RCP2.6 is dominated by the peak RF-forced ocean slow response through 2300. Indeed, the evolution of this deep ocean warming structures is also confirmed in 24 models from RCP2.6 through 2100 and in 14 models from RCP4.5 through 2300 (Fig. S1 in the online supplemental material.). It is worth noting that the ocean warming penetrates deeper in RCP2.6 than RCP4.5, as indicated by the depth of the maximum ocean warming (around 500 m in RCP4.5 vs 1000 m in RCP2.6). This difference in deep ocean warming structure between the two scenarios is indicative of both the ocean

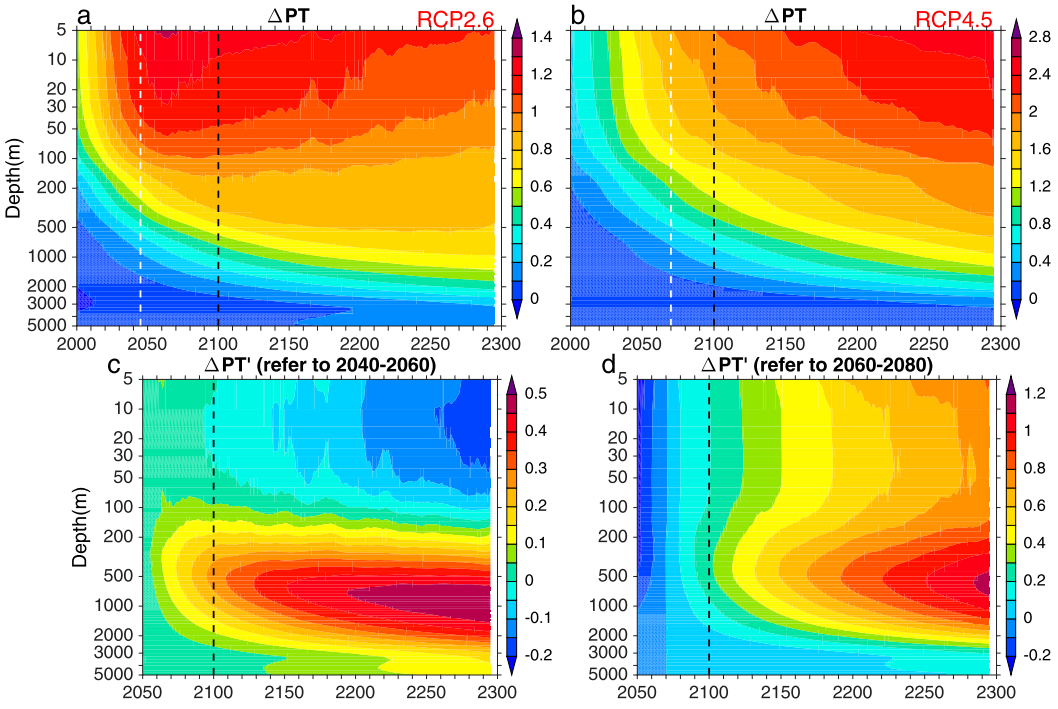

FIG. 3. Time evolution of ensemble-mean and global-mean ocean potential temperature change (ΔPT) profile in (a),(c) RCP2.6 and (b),(d) RCP4.5 from the ensemble mean of eight models with extension simulations (Table 1) at all depths, based on 11-yr running means. Changes of PT (ΔPT) in (a) and (b) and further changes of PT (ΔPT′) in (c) and (d) are relative to the preindustrial period and the period centered at the RF inflection point, respectively. The white dashed line indicates the RF inflection point. Note that the vertical depth coordinates are logarithmic.

fast and slow cooling responses to the negative RF deviating from the peak RF.

The enhanced deep ocean warming generally weakens the vertical temperature gradient after the RF inflection point and hence acts as an indirect warming feedback on surface and upper ocean warming by reducing downward heat transfer. This explains why upper ocean cooling is weak when RF declines, in contrast to the rapid warming during the RF increase period. The indirect deep ocean feedback also affects the global-mean and surface climate response due to the regional differences in its magnitude associated with ocean dynamics (Held et al. 2010; Chadwick et al. 2013; Long et al. 2014, 2018).

a. Global-mean temperature response

Figure 4 shows GMST changes, with the blue and black thick lines indicating results from different numbers of ensembles. The variation in the number of models used in the ensemble mean causes only small variations in global-mean response. This give us confidence in the results from the eight models that have extended simulations through 2300. Particularly, the global-mean surface temperature change is about 1.8°C at 2100 in RCP2.6, in line with the 2°C warming target.

In both RCP2.6 and RCP4.5, GMST increases rapidly with RF (red thick line in Fig. 4) in the first half of the twenty-first century and is dominated by the fast warming component (Held et al. 2010; Long et al. 2014). After the RF inflection point, GMST ramps down slowly in RCP2.6 (Fig. 4a), whereas it continues to increase at a slower rate than the RF increase period in RCP4.5 (Fig. 4e). We apply the diagnostic method introduced in section 2c to separate the post-RF peak change in GMST into a slow warming component due to ocean slow response with constant peak RF and a cooling component due to negative RF (Fig. 5). The cooling component consists of a fast cooling component due to fast mixed layer response and a slow cooling component due to ocean slow response under negative RF. When RF decreases in RCP2.6, the fast cooling component (Tn_f; blue line) develops over time that reduces the fast warming component produced during the RF increase period, leading to a decline in total fast component and hence its percentage contribution to the total GMST rise (Fig. 4e). In contrast, the ocean slow response with constant peak RF leads to a persistent increase in the slow warming component of GMST change (Tp_s; red line), from about 0.2°C by 2100 to 0.6°C by 2300 (Fig. 5a, red line). As a result, the percentage contribution of Tp_s

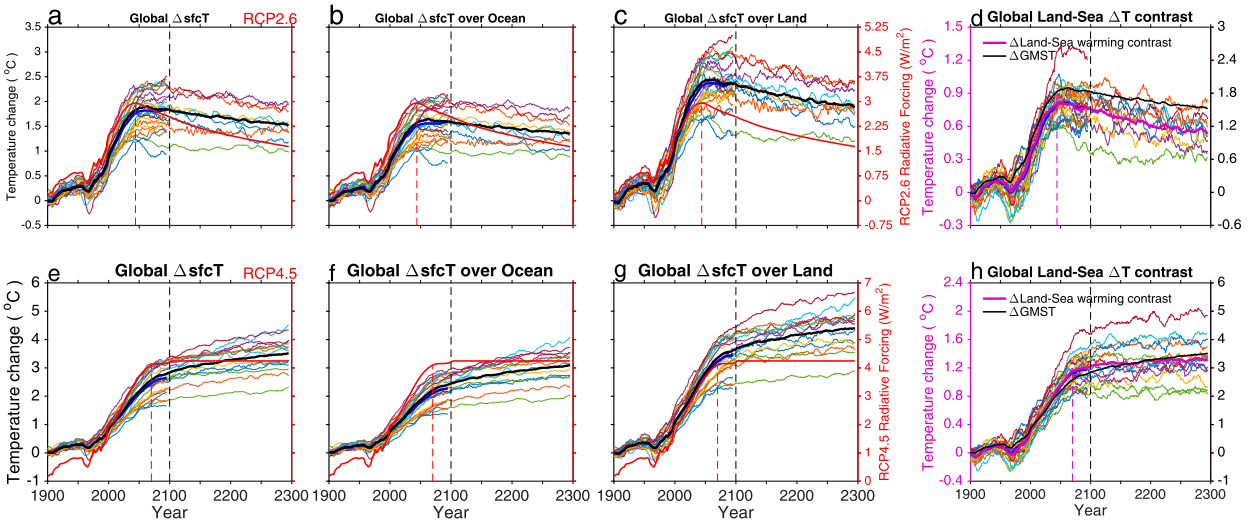

FIG. 4. Prescribed radiative forcing pathway (red thick line) and global-mean change (denoted as Δ, relative to the 1850–99 mean) of (a),(e) surface air temperature (sfcT), (b),(f) ocean sfcT, (c),(g) land sfcT, and (d),(h) land–sea warming contrast (magenta line) for (top) RCP2.6 and (bottom) RCP4.5. All results are based on 11-yr running means. Colored thin lines indicate the results of each model, while the blue and black thick lines respectively indicate ensemble-mean results from 24 models and 8 models. The vertical red and black dashed lines present the year when RF reaches the peak and 2100, respectively.

to total GMST warming increases from 10% in 2100 to above 40% in 2300 (Fig. 5b). The slow cooling response to RF decline (Tn_s; green line) also develops over time, playing a relatively small but not negligible role (less than 10% by 2300). Moreover, the signal-to-noise ratio (SNR), defined as the ensemble-mean divided by the intermodel standard deviation, of the slow warming component is above 2.5 through 2300, illustrating the consistency of the estimation across models. Particularly, the results at the end of the twenty-first century are also supported by the ensemble mean of 14 models (diamonds in Fig. 5), suggesting the robustness of the scaled results.

The GMST trajectory is nearly flat at 1.87°C during 2050–2100 in RCP2.6, mainly resulting from the offset between the cooling component and slow warming component. It then declines slowly to about 1.5°C by 2300 as the cooling component slightly exceeds the slow

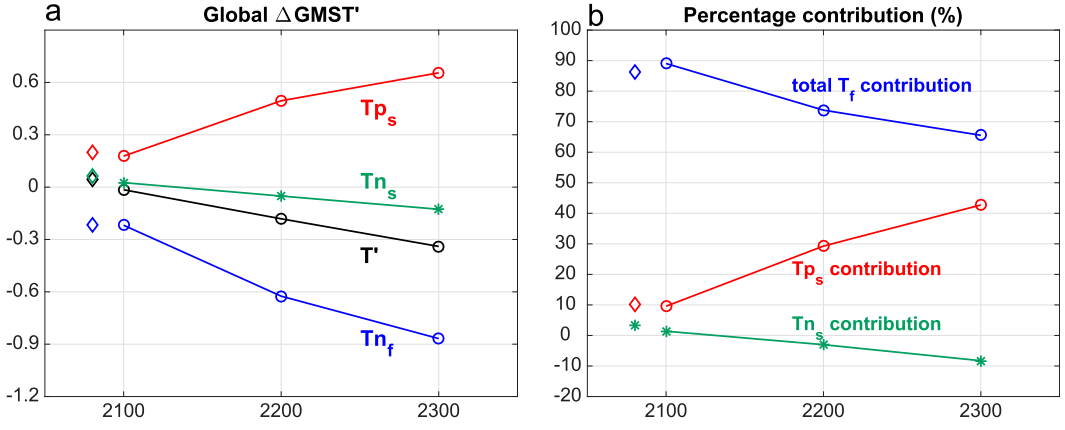

FIG. 5. (a) Post-RF peak changes of GMST (T') change (black line) and its fast cooling component (Tn_f; blue line), slow cooling component (Tn_s; green line), and the peak RF-forced slow warming component (Tp_s; red line) based on results from eight models in RCP2.6. (b) The percentage contribution to total change from different components. Note that the total fast component is the sum of the fast warming component during RF increase period and the fast cooling component during RF decrease period. The sign of the slow warming component is always positive as the deeper ocean continually warms. Circle (diamond) markers indicate results based on 8 (14) models with RCP extension simulations available.

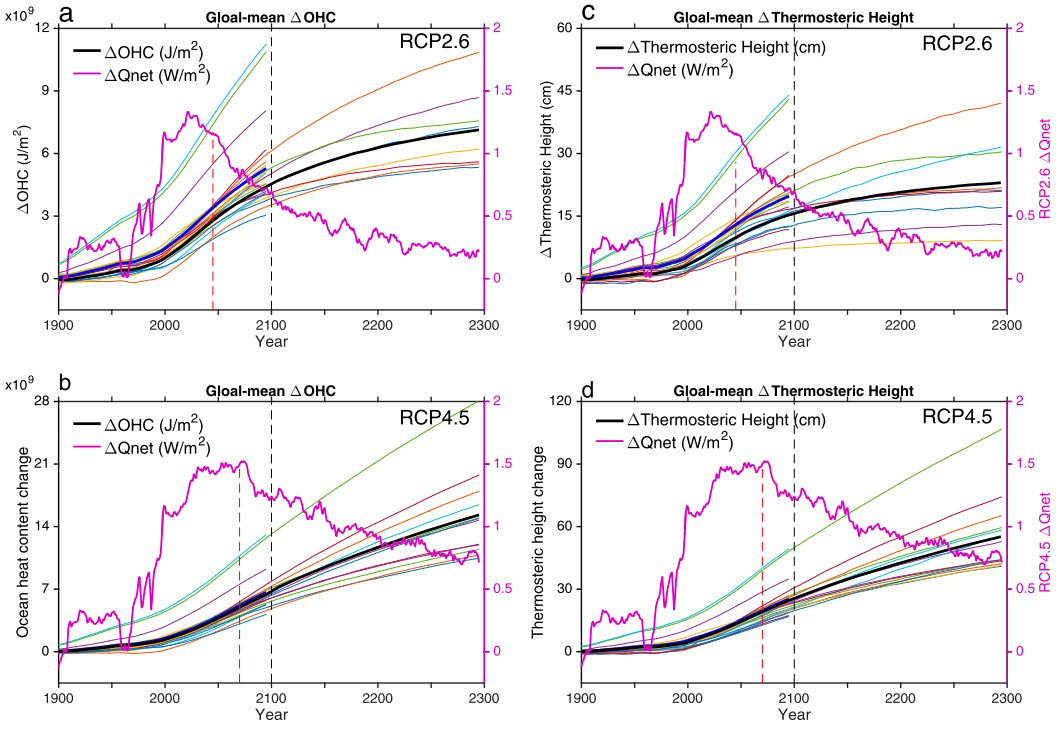

FIG. 6. Global-mean (a),(b) ocean heat content (OHC) change and (c),(d) thermosteric height change along with change in global-mean (60°S–60°N) surface heat flux (eight-model ensemble-mean ΔQnet) into ocean (purple thick line corresponding to the vertical right axis) in (top) RCP2.6 and (bottom) RCP4.5. The blue and black thick lines indicate ensemble-mean results from 24 and 8 models, respectively.

warming component (Fig. 5a). These results suggest that the deep ocean feedback (slow warming component) with constant peak RF and the cooling component due to negative RF jointly shapes the trajectory of GMST change. This has important implications for selecting possible ways to achieve the 1.5° or 2°C warming targets.

Global-mean ocean and land surface temperature both largely follow the GMST trajectory but differ in the rate of change due to a much smaller heat capacity of land (Fig. 4). The land–sea thermal contrast, defined as the difference between global-mean temperature of land and ocean surface, rises rapidly when RF increases due to much faster warming over land than ocean (Figs. 4d,h). When RF ramps down in RCP2.6, the percentage decrease of land–sea thermal contrast is larger than that in GMST (Fig. 4d) as land surface cools faster than ocean surface. It helps to narrow the warming gap between land and ocean surface. In RCP4.5, the thermal contrast still increases slowly after the RF inflection point, suggesting that ocean slow response also favors a faster surface warming over land than ocean (Fig. 4h). The discrepancy in the land–sea thermal contrast changes after the RF inflection point between RCP2.6 and RCP4.5 is primarily attributed to the declining RF.

b. *Ocean heat content and sea level*

Under global warming, ocean absorbs 93% of Earth's energy imbalance (Rhein et al. 2013; Trenberth et al. 2014), resulting in robust increases in global-mean ocean heat content (OHC) and sea level (Cheng et al. 2019). The slow but unceasing deep ocean warming after the RF inflection point is because the surface net heat flux into the ocean stays above preindustrial level (Fig. 6; purple line). It follows that global-mean OHC increases persistently and only slows its rate of increase when RF ramps down in RCP2.6 (Fig. 6a), consistent with the result from the simple two-box model in Fig. 2b. Thermosteric sea level rise due to thermal expansion of seawater largely resembles the global-mean OHC change trajectory. As a result of the accumulated heat in ocean, global-mean OHC and sea level change display much smaller natural variability with robust increase trends across models compared with other variables.

The results of this section show that the ocean slow response with constant peak RF has profound effects on global-mean responses. As the magnitude and vertical structures of the deep ocean warming both vary across basins, they further cause regional variations in surface warming and ocean–atmosphere coupling processes,

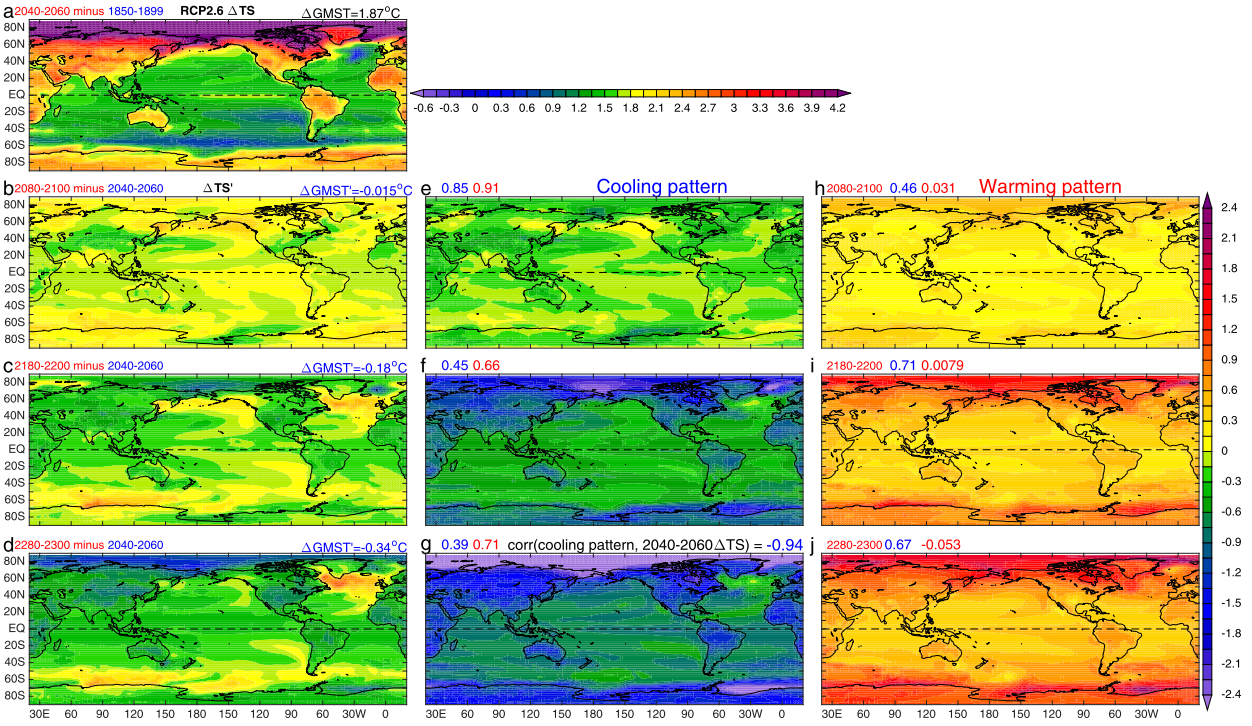

FIG. 7. Multimodel ensemble-mean results in RCP2.6 for (a) surface temperature change (ΔTS) during the RF increase period in 2040–60 referenced to 1850–99. (b)–(d) Post-RF peak change (relative to 2040–60) in surface temperature (ΔTS′) and (e)–(g) its cooling component (Tn_f + Tn_s) pattern and (h)–(j) its warming component (Tp_s) pattern decomposed based on our diagnostic method. The global-mean surface air temperature change (ΔGMST) at each period is shown at top right of (a)–(d); the prime indicates change referenced to 2040–60. Note that the upper color bar is only for Fig. 7a. The color numbers labeled at the top of (e)–(j) are spatial correlation coefficients between the subcomponent's pattern and ΔTS' pattern within 60°S–60°N for ocean (blue) and land (red) surface.

shaping spatial patterns of climate response (Shi et al. 2018; Chen et al. 2019).

4. Spatial pattern change

a. *Surface temperature pattern*

Figure 7 shows multimodel ensemble-mean surface skin temperature change (ΔTS, SST over ocean) in RCP2.6 during four periods, along with the patterns of warming and cooling components obtained by our diagnostic method. During 2040–60, the surface warming (referenced to 1850–99) pattern closely resembles that in the higher emission scenarios, such as the hemispheric difference, land–sea contrast, equatorial zonal structures, and the reduced warming over the Southern Ocean and North Atlantic (Xie et al. 2010; IPCC 2013).

Figures 7b–d display patterns of surface temperature change relative to 2040–60 (denoted as ΔTS′) to illustrate the pattern changes after the RF inflection point. Because RF remains constant at its peak value in RCP4.5, its changes after the RF inflection point are fully due to ocean slow response (Long et al. 2014; slow warming pattern). By applying our diagnostic method and considering the difference in the RF inflection point, we can obtain the warming and cooling patterns for ΔTS′ in RCP2.6. The cooling pattern consists of a fast cooling response pattern and a slow cooling response pattern to the negative RF. Despite limitations in the diagnostic method, it gives us qualitative, and to some extent quantitative, information about underlying processes for surface pattern evolution.

During 2080–2100, global-mean surface temperature change (ΔGMST′) is rather small (−0.015°C) (Fig. 7b), as the slow warming opposes the RF decline-induced cooling (Fig. 5a; Figs. 7e,h). Natural variability may cause substantial uncertainty in the post-RF peak changes before 2100. The effect of the deep ocean feedback on surface warming (slow warming component) is first visible over the mid- to high-latitude oceans (Fig. 7h). In the early stage after the RF inflection point (2080–2100), the ΔTS′ pattern between 60°S and 60°N is mainly dominated by the cooling pattern, with the spatial correlation exceeding 0.85 for both ocean and land (numbers labeled at top left in Fig. 7e, with blue for ocean and red for land).

During the twenty-second and twenty-third centuries, the total warming further weakens (Figs. 7c,d) as the negative RF effect (Figs. 7f,g) outweighs the slow warming

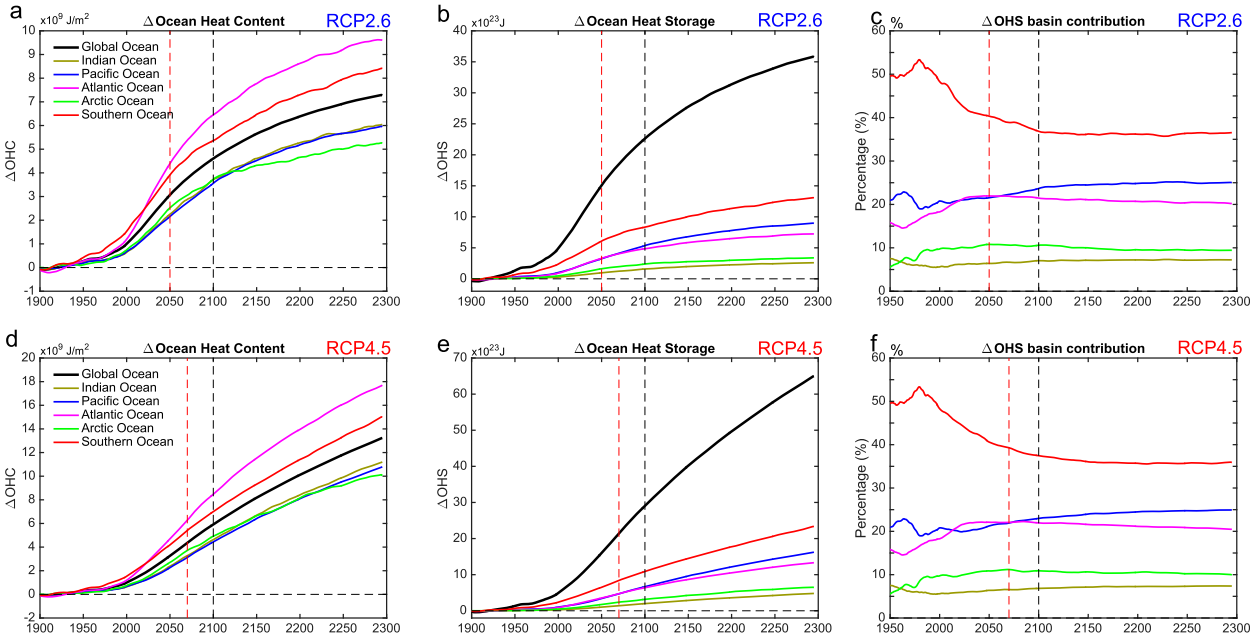

FIG. 8. Time series of (a),(d) area-weighted-mean ocean heat content change (ΔOHC; relative to 1850–99), (b),(e) area-weighted-integrated OHC change (ocean heat storage change, ΔOHS) of global ocean and different basins, and (c),(f) percentage contributions from each basin for (a)–(c) RCP2.6, and (d)–(f) RCP4.5. All results are based on 11-yr running means.

effect (Figs. 7h,l). However, there is still noticeable warming over the Southern Ocean, southern subtropics, and North Atlantic by 2300 despite considerable reduction in RF (about $-1.4\,\mathrm{W\,m^{-2}}$). The $\Delta TS'$ pattern is consistent with the results from a CO_2 removal experiment from a single model (Chadwick et al. 2013). Globally, the slow warming pattern with constant peak RF increases over time and leads to continuous warming over all regions, especially in the mid- to high latitudes where the large ocean dynamical effects (Fig. S2) allow a strong deep ocean feedback (Held et al. 2010; Xie et al. 2010; Long et al. 2014). As expected, the cooling pattern also increases over time and nearly offsets the surface warming during 2040–60. The spatial correlation between the fast cooling component during 2280–2300 and the surface warming during 2040–60 is −0.94, further confirming their similarity. It implies that the climate response under the RF change scenario, like GHG increase or anthropogenic aerosol emissions, is first dominated by the fast ocean mixed layer adjustment, so it is to first order similar in spatial structure with a sign difference (Xie et al. 2013, 2015). Therefore, understanding climate change during the RF increase period can help to improve the projection on the surface cooling response to RF decrease. However, the climate response under low warming scenarios includes an additional ocean slow response with constant RF (i.e., the $\Delta TS'$ pattern in RCP4.5). Globally, the slow warming pattern overwhelms the cooling pattern in shaping the $\Delta TS'$ pattern within 60°S–60°N through 2300, especially in the mid- to high-latitude oceans. In contrast, the spatial structures of surface temperature change over land and polar regions are mainly dominated by the cooling component, consistent with the global-mean land–sea warming contrast change.

The results of decomposition highlight that ocean slow response can persistently influence long-term surface temperature change, which is important for atmospheric circulation and precipitation responses (Xie et al. 2015; Long et al. 2016) and climate variability (Zheng et al. 2019). Furthermore, the results also imply that once the accumulated anthropogenic carbon emission reaches a high level, substantial mitigation effort to achieve negative carbon emissions is demanded to offset the surface warming from ocean slow response and keep GMST rise at a low level.

b. Ocean heat content pattern

The OHC change is a robust indicator of the global warming (Levitus et al. 2012; Cheng et al. 2019; Liu et al. 2016). Its pattern is a result of the balance between local heat uptake and ocean heat redistribution. Figure 8 shows the evolution of area-integrated-mean OHC change of global ocean and in five major basins. OHC increase is noticeable in all basins after the Industrial Revolution, with reduced rate when RF decreases or stabilizes (Figs. 8a,d). However, the area-weighted mean OHC increase is much larger in the Southern

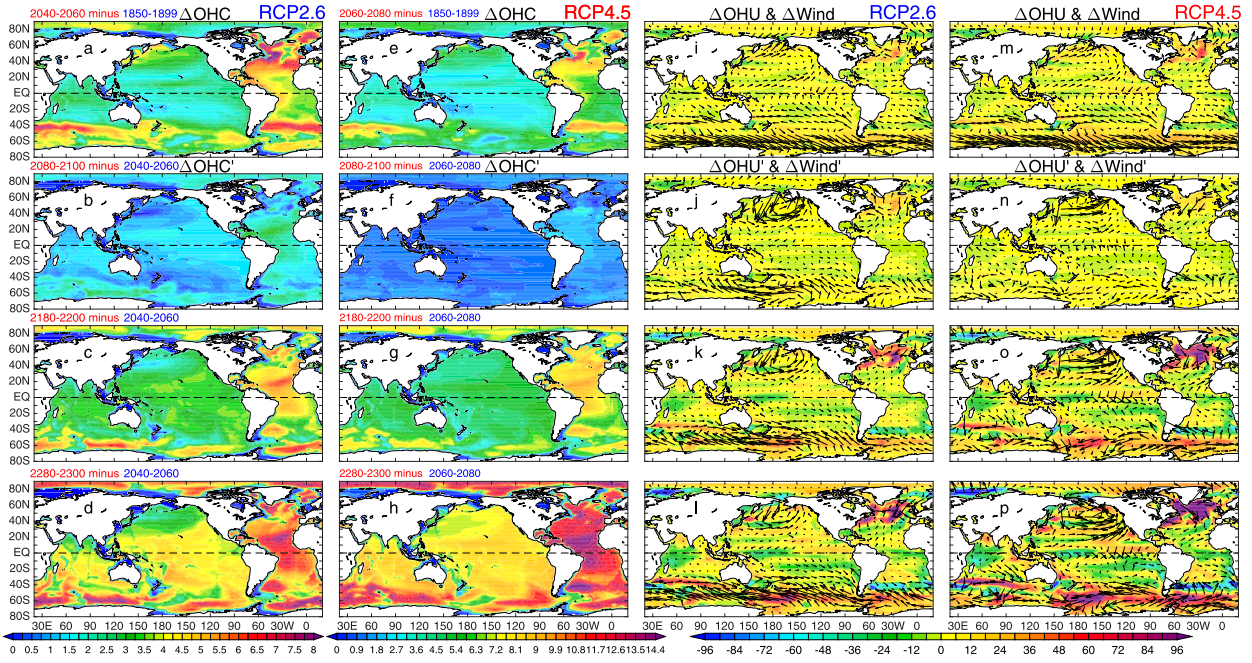

FIG. 9. Global ocean heat content change at four periods for (a)–(d) RCP2.6 and (e)–(h) RCP4.5, and time-integrated surface heat flux (color shading) and surface wind stress change (vectors) for (i)–(l) RCP2.6 and (m)–(p) RCP4.5. Note that results in the second to fourth rows are referenced to 2040–60 and 2060–80 in RCP2.6 and RCP4.5, respectively.

Ocean and Atlantic Ocean than other basins, which is primarily because ocean heat uptake is the most active over these two regions (Fig. 9). Moreover, the Southern Ocean plays a dominant role in global OHS before 2000 (Figs. 8b,c). The percentage contribution of the Southern Ocean to global OHS increase reaches about 50% before 2000 but declines to around 40% by 2050 and 35% by 2100 (Fig. 8c), suggesting a compensate contribution from other basins. This is mainly explained by an increased contribution from the Atlantic, especially before 2050. Shi et al. (2018) show that, historically, anthropogenic aerosols' cooling effect is the most pronounced in reducing the North Atlantic Ocean surface heat uptake and hence Atlantic OHC increase. After 2000, as the atmospheric aerosols concentration gradually decreases, its cooling effect also reduces (Shi et al. 2018). This would accelerate the Atlantic OHC increase in addition to the effect from the increase in GHGs concentration, making the OHC increases much faster in the Atlantic than all other basins (Fig. 8a). Indeed, the Atlantic OHS is comparable to that of the Pacific Ocean despite a much smaller area.

After 2100, percentage contributions from all basins stay nearly constant (right panels), with slightly increased contribution in the Pacific Ocean and decreased contribution from the Atlantic Ocean. The increased contribution from the Pacific is possibly a result of anomalous heat import from other basins through the global conveyor belt as suggested by Garuba and Klinger (2016). Results from RCP4.5 are similar but with higher rate of OHC increase (Fig. 8d) after the RF inflection point compared to those in RCP2.6 (Fig. 8a), indicating that most of the OHC increase and its spatial distribution in RCP2.6 are still dominated by ocean slow response with constant peak RF despite a substantial decline in RF after 2045.

Spatially, OHC increase is the most prominent around 45°S over the Southern Ocean and North Atlantic Ocean in both RCP2.6 and RCP4.5 (Figs. 9a,e). Moreover, there is also enhanced OHC increase in the North Pacific Ocean, especially north of 40°N, accompanied by a locally enhanced surface warming (Fig. 7a). This surface warming cannot be attributed to ocean dynamical effects (Figs. S2a,e) but is associated with a decrease in wind speed due to weakened Aleutian low pattern (Figs. 9i,m) (Xie et al. 2010; Long et al. 2014). Previous studies suggest that the larger OHC increase in the subpolar than in the subtropical Pacific is associated with gyre circulation change (Winton et al. 2013; Garuba and Klinger 2018).

Despite RF decrease, further increase in OHU referenced to 2040–60 is still prominent through 2300 in the North Atlantic and Southern Ocean (Fig. 9b). Correspondingly, the magnitude of their surface heat uptake is also larger (Fig. 10) than the global-mean value (Fig. 6), along with a striking air–sea warming contrast over both

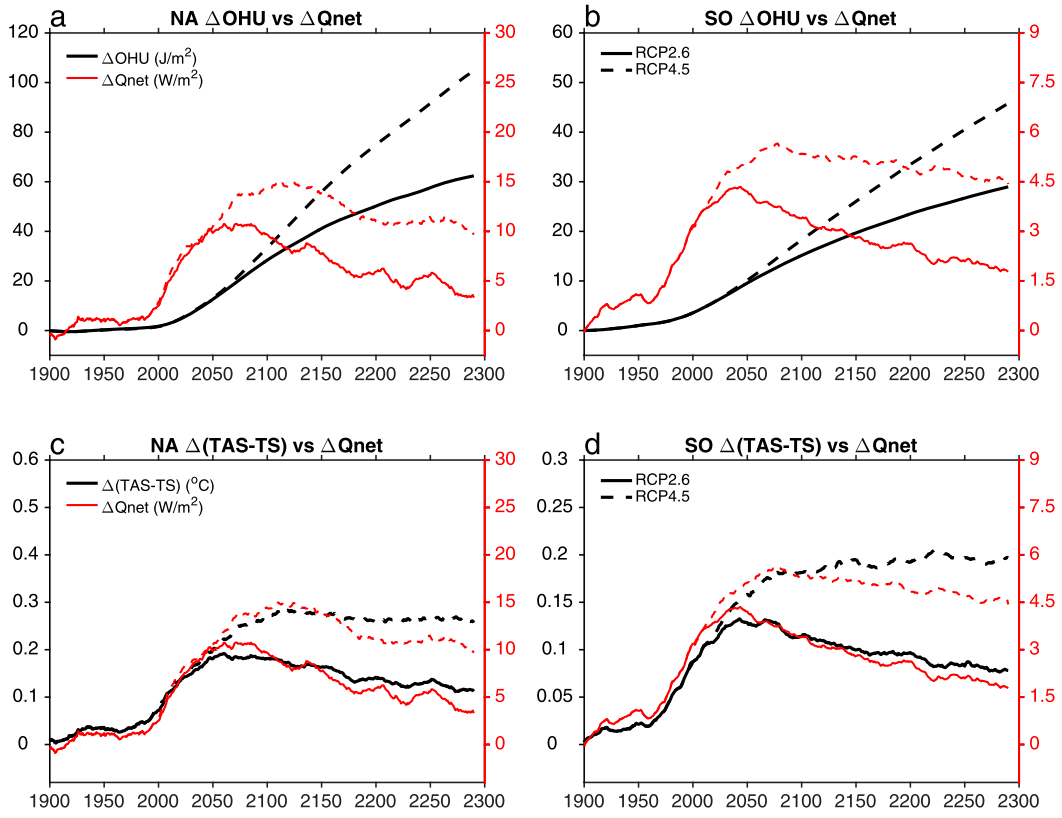

FIG. 10. Time series of area-weighted-mean surface heat flux change (ΔQnet) along with (a),(b) area-weighted-mean ocean heat uptake change (time integration of ΔQnet, ΔOHU) and (c),(d) air–sea warming contrast (ΔTAS minus ΔTS) in the (left) North Atlantic (NA; 40°–60°N, 60°W–0°) and (right) Southern Ocean (SO; 65°–45°S, 0°–360°) based on eight models, with the solid lines for RCP2.6 and dashed lines for RCP4.5.

regions (Fig. S3). Here the air–sea warming contrast, Δ(TAS − TS), is defined as total change in ocean surface air temperature minus SST referenced to 1850–99. Indeed, this contrast remains positive over these two regions through 2300 (Fig. 10), suggesting that the atmosphere continues to warm the ocean (Fig. S3). This sustains the long-lasting OHU and hence persistent OHC increase.

In contrast, the North Pacific OHC increase lags behind other oceans, especially over latitudes between 30°–60°N, and is associated with a strengthened Aleutian low pattern (Figs. 9j–l). The reduced rate of OHC increase over the North Pacific is also visible in RCP4.5 (Figs. 9g,h) but with a weakened magnitude and is displaced southward, together with the shift in the wind stress change pattern. In RCP2.6, OHC increase is locally reduced along the Gulf Stream during 2180–2200 and 2280–2300 (Figs. 9c,d), which is absent in RCP4.5 (Figs. 9g,h) and mainly attributed to the gradually recovered AMOC in response to RF decrease. The recovered AMOC in RCP2.6 would intensify northward heat transport and reduce heat uptake, mainly above 500 m (Figs. S4b,c), along the Gulf Stream. Besides, the heat absorbed over the subpolar North Atlantic gradually spreads out to the whole basin. In the Southern Ocean, regions of prominent OHC increase move poleward in both RCP2.6 and RCP4.5, while the maximum OHU still stays around 60°S.

Indeed, global OHC increase after the RF inflection point mainly follows the deep ocean warming at depth of 500–3000 m (Fig. 3; see also Fig. S4). The regional OHC change pattern is determined by surface heat uptake and heat redistribution by ocean circulation (Gregory 2000; Xie and Vallis 2012; Winton et al. 2013; Garuba and Klinger 2016, 2018; Liu et al. 2016, 2018).

5. Processes for deep ocean warming

a. Ocean warming during RF increase period

This section examines the zonal-mean ocean responses in three major basins: the Southern Ocean, Atlantic Ocean, and Indo-Pacific Ocean (Fig. 11). During 2040–60 (the first row in Fig. 11), the upper ocean warming in the Southern Ocean is mainly trapped within the Deacon cell above 1500 m and is primarily associated

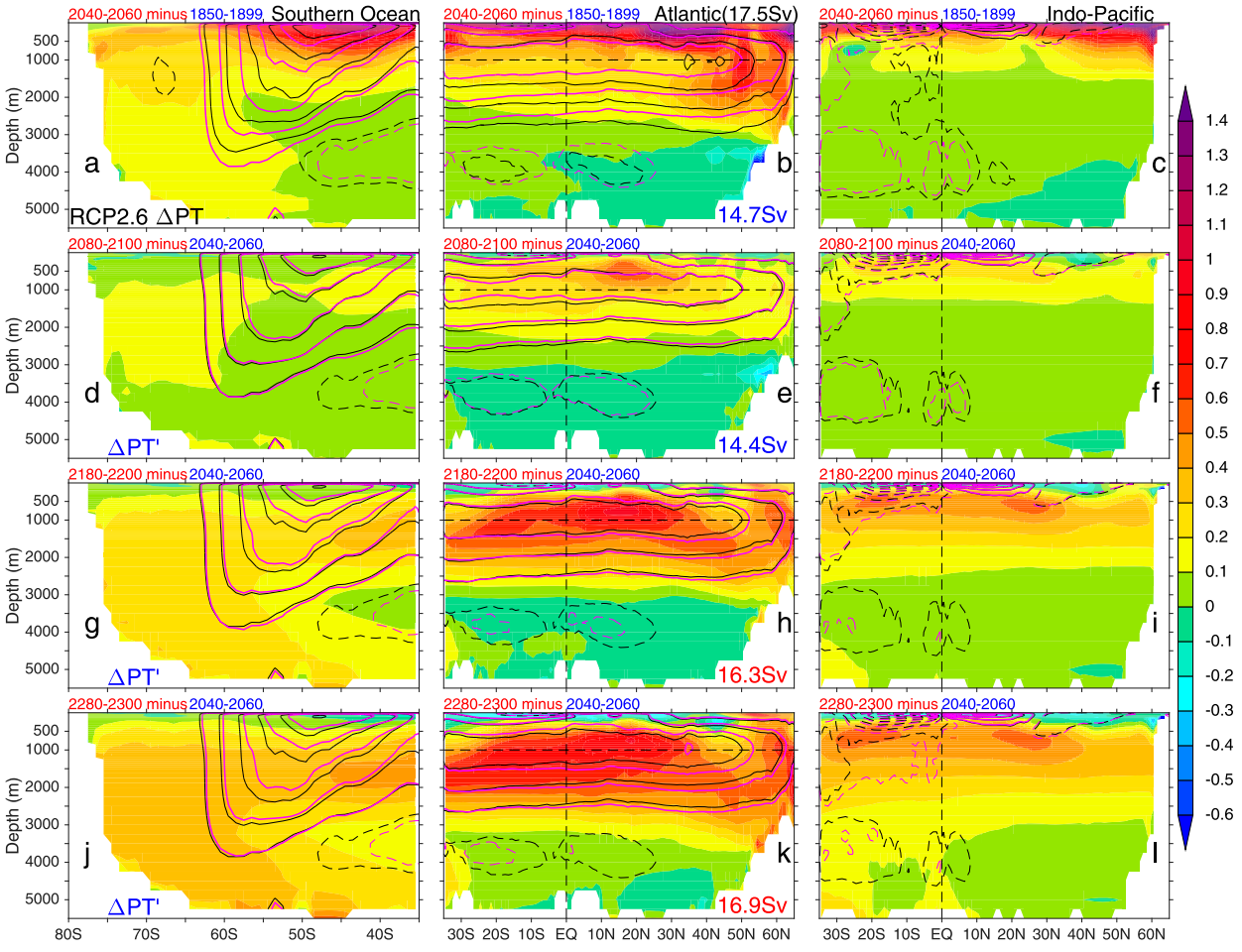

FIG. 11. Ocean temperature change (ΔPT; color shaded) and climatology MOC (contours, with black lines for the referenced period) from different basins during four periods in RCP2.6. The postpeak changes (ΔPT′) in the last three periods are relative to 2040–60 mean.

with the climatological Eulerian-mean MOC (Liu et al. 2018). Specifically, heat absorbed by the upwelled cold water around 60°S (contours in Fig. 11a) is transported northward by climatological Ekman flow, causing a prominent heat storage around 45°S (Fig. 9a) (Marshall et al. 2015; Garuba and Klinger 2016; Morrison et al. 2016; Liu et al. 2018). Therefore, the location of maximum OHC increase is also accompanied with locally enhanced surface warming around 45°S, in contrast to that in the subpolar North Atlantic where surface warming is largely reduced (Fig. 7a; see also Figs. S2a,e). Under increased RF, ocean warming is mainly confined to the upper 500 m in the Indo-Pacific Ocean and south of 30°N in the Atlantic Ocean. The enhanced warming signal (>0.2°C) extends to 2000 m in the subpolar Atlantic, much deeper than that in the Indo-Pacific Ocean.

The Atlantic Ocean displays the most prominent ocean warming with the deepest penetration due to the AMOC. Both climatology and the weakening of the AMOC are important in Atlantic Ocean warming (Xie and Vallis 2012; Winton et al. 2013; Marshall and Zanna 2014; Garuba and Klinger 2016). Here the AMOC is shown in contours and the AMOC index labeled at the bottom right of the Atlantic panels in Fig. 11. The climatological AMOC transports anomalous upper-ocean heat northward, causing heat to pile up north of 30°N, with the warming signal penetrating into great depths [see Fig. 5 in Marshall et al. (2015) and Fig. 2 in Garuba and Klinger (2016)]. By contrast, the AMOC weakens and shoals in response to RF increase (Fig. 11b, contours), reducing SST warming north of 30°N in the North Atlantic Ocean (Russell and Rind 1999; Kim and An 2013; Rugenstein et al. 2013; Liu et al. 2017; Sévellec et al. 2017; Liu and Fedorov 2019) (Fig. 7a) and enhancing ocean heat uptake from the atmosphere (Figs. 9i,m). As a result, the warming magnitude of the North Atlantic Ocean between 500 and 3000 m increases (Fig. 11b) (Garuba and Klinger 2016). Moreover, the large upper-ocean warming north of 40°N in the North

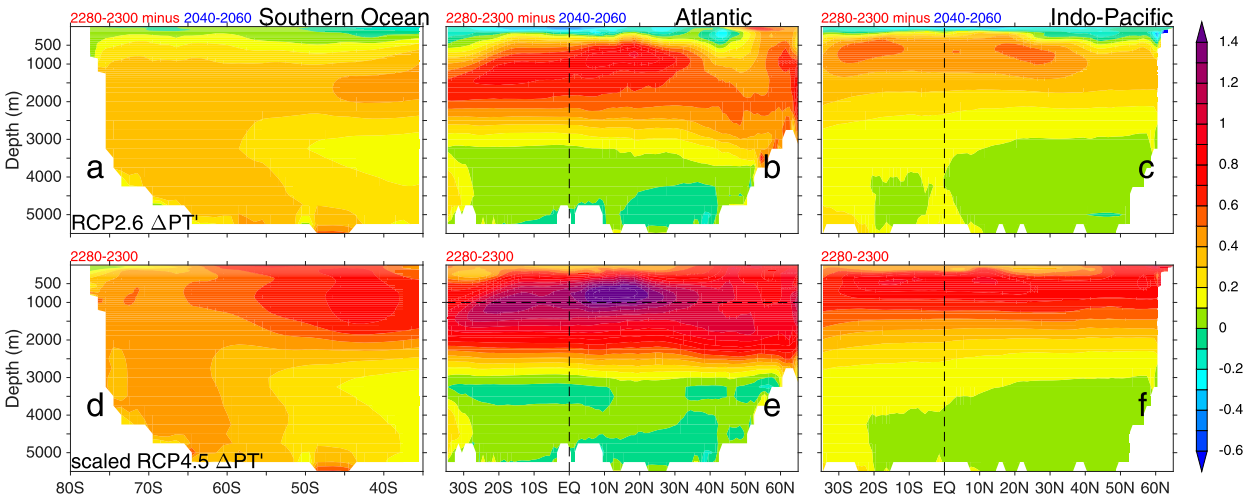

FIG. 12. Zonal-mean profiles in three basins for ocean potential temperature (a)–(c) post-RF peak changes during 2280–2300 (ΔPT′, referenced to 2040–60) in RCP2.6 and (d)–(f) the scaled slow warming component from RCP4.5.

Pacific Ocean also penetrates into a relatively deep layer of around 1000 m, which is associated with both circulation change and the vertical mixing and diffusion due to weak and shallow stratification there (Fig. S5).

b. Ocean warming during RF decrease period

When RF decreases, ocean further warms below 200 m but cools above in all basins (referenced to 2040–60, second to fourth rows in Fig. 10), consistent with the global-mean results (Figs. 3c,d). The deep ocean warming generally intensifies over time and extends downward. As discussed in the previous sections, further changes after the RF peak in RCP2.6 can be viewed as a combination of slow warming response with constant peak RF and cooling response to negative RF. Figure 12 shows the post-RF peak changes in potential temperature (ΔPT′) during 2280–2300 in RCP2.6 and the scaled ΔPT′ from RCP4.5 (slow warming response). The two sets of results resemble each other in the overall ocean warming structure below 500 m, indicating the importance of the ocean slow response with constant peak RF through 2300. The difference between them is mainly due to negative RF effect (cooling response). It clear that the upper ocean would substantially cool at all latitudes above 2500 m due to RF decrease, especially in the upper 500 m. As a result, in the total warming profile referenced to preindustrial (Fig. S6), the warming magnitude of layer above 2500 m is more evenly distributed during 2280–2300 than that during 2040–60.

To be specific, in the Southern Ocean, there is prominent warming south of 50°S extending from 500 m to the bottom and spreading equatorward (Fig. 12d). It is dominated by the ocean slow response with constant peak RF like RCP4.5 (Fig. 12d). Although this upper-to-bottom warming structure is evident in nearly all 14 models with RCP4.5 extension simulation, it also displays substantial differences in the magnitude and detailed pattern across models (Fig. S7). This may occur because the Southern Ocean deep-layer temperature change involves complex processes associated with effects from surface heat flux, wind stress, freshwater flux, and so on (Bitz et al. 2006; Gregory et al. 2016; Liu et al. 2018). Further studies to quantify individual contributions from different factors and well explain underlying mechanisms are needed. This upper-to-bottom ocean warming structure explains why the location of the maximum OHC increase in the Southern Ocean moves southward from around 45° to 60°S in both RCP2.6 and RCP4.5 (Figs. 9a–h). In comparison, the deep ocean warming above 3000 m north of 50°S is dominated by the intensified ocean warming within the Deacon cell, mainly a result of the persistent OHU that peaks around 60°S (Figs. 9i–p). Eddies in the Southern Ocean generally induce MOC change opposite to the Eulerian-mean change (Fig. S8), consistent with Liu et al. (2018). As a result, albeit relatively small in magnitude, eddies would weaken the OHC change (Fig. S9). The eddy effect is important on the northward heat transport north of 45°S, however, and further studies are needed.

In the Atlantic, the enhanced subsurface warming is mainly trapped within the AMOC (Figs. 11e–k), different from the case in the Indo-Pacific Ocean where the warming deepens even without a deep MOC (Figs. 11f–l). This implies substantial interbasin differences in the dynamics of the deep ocean warming. In the ocean slow response with constant peak RF, AMOC change is weak (0.27 Sv) and so the air–sea contrast in surface warming (Fig. 13b) and hence OHU remains strong over the

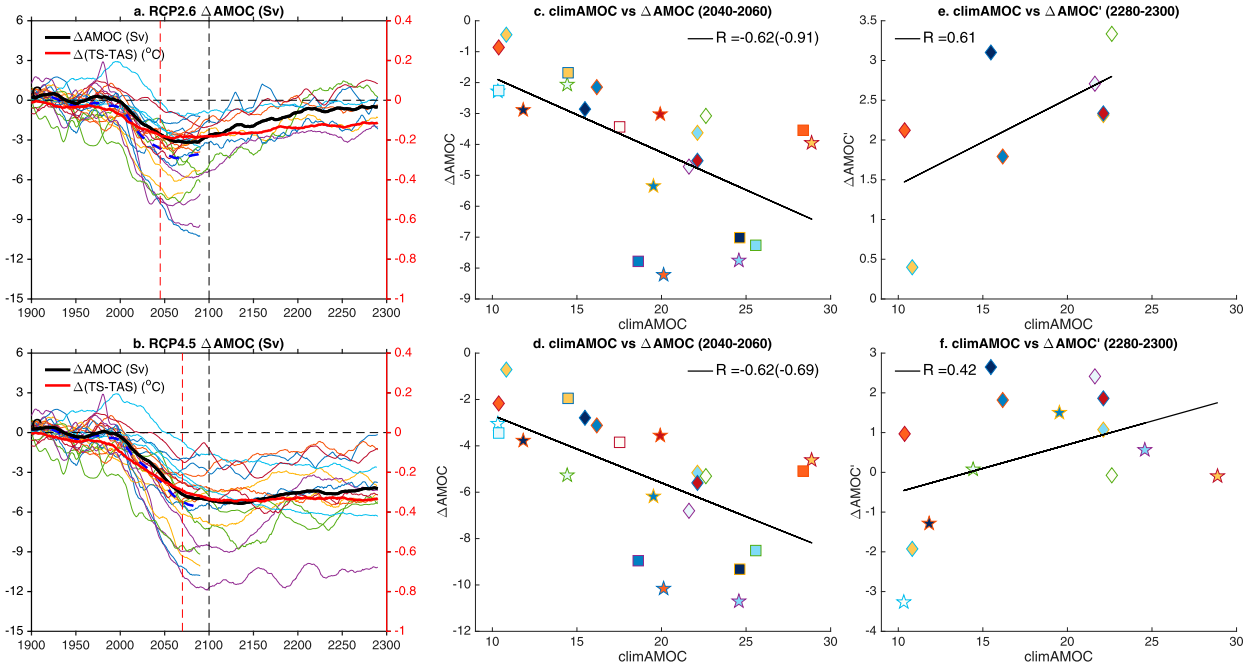

FIG. 13. (a),(b) Time series of the AMOC index along with difference in surface temperature between sea and air [red thick line, Δ(TS − TAS)], in RCP2.6 and RCP4.5, respectively, and scatterplots of climatology AMOC vs (c),(d) AMOC change (ΔAMOC) during RF increases period referenced to 1850–99 and (e),(f) AMOC change during 2280–2300 (denoted as ΔAMOC′) respectively referenced to 2040–60 and 2060–80 in RCP2.6 and RCP4.5. The correlation coefficient between the climatology AMOC and AMOC change is labeled at the top of (c)–(f), with the number in the parentheses indicating the coefficient for 8 models and 14 models with extension simulations in RCP2.6 and RCP4.5, respectively.

North Atlantic (Fig. 10a), resulting in pronounced deep ocean warming over the Atlantic Ocean. In contrast, AMOC recovers and gradually strengthens when RF declines (Fig. 13a), along with a decrease in the air–sea warming contrast, leading to substantial cooling above 2000 m and small warming below in the fast component (Fig. 12). As a result, the Atlantic deep ocean warming is considerably reduced in magnitude but penetrates deeper in RCP2.6. Sea surface warming remains smaller than surface air over the North Atlantic (Fig. 13), allowing a persistent ocean heat uptake. The trajectory of sea–air surface temperature difference largely follows the AMOC change in both RCP2.6 and RCP4.5, suggesting the dominant role of AMOC change in North Atlantic heat uptake.

The slowdown of the AMOC to RF increase is robust across models and scenarios (Fig. 13). After the RF peak, the AMOC recovery is evident after 2100 and also consistent among models (Fig. 13a). This AMOC recovery is mainly due to the feedbacks related to surface heat flux and surface salinity change (Shi et al. 2018; Wen et al. 2018; Haskins et al. 2019; Liu et al. 2019). Particularly, differences in the AMOC change across models are tightly associated with the climatological AMOC, consistent with previous studies (Gregory et al. 2005; Weaver et al. 2007). The AMOC weakens more in response to RF increase in models with a stronger climatological AMOC (Figs. 13c,d). This may be explained by an energetic argument that models with a stronger present-day AMOC tend to have a larger reduction in the generation of kinetic energy in a warming climate and hence more suppression in deep convection activity (Gregory and Tailleux 2011). Besides, models with a weaker climatology AMOC are of a more intensified stratification over deep-water formation region, which would restrain changes in deep convection and AMOC (Sgubin et al. 2017). Likewise, intermodel differences in the AMOC recovery are also positively correlated with the intermodel spread in the intensity of mean AMOC (Figs. 13e,f), which has not received much attention and is worth future study. These results highlight the influence of the climatological AMOC in future AMOC change and hence long-term ocean evolution. It also implies that an improved simulation in present-day AMOC would help reduce uncertainty in projecting future AMOC change and associated climate effects (Chen et al. 2019).

6. Summary and discussion

We have investigated the role of ocean slow response under low warming targets using RCP2.6 and RCP4.5

simulations in the CMIP5 ensemble. The deep ocean warms much more slowly than the upper ocean when RF increases but then warms faster than the upper ocean when the RF increase ceases (Fig. 1). The continuing deep ocean warming after the RF inflection point is a robust feature of ocean slow response and has clear feedback on surface climate change. A diagnostic method is applied to separate the effect of the continuous deep ocean warming under low warming scenarios with RF decrease. Based on the results from RCP4.5, we decompose the RF evolution into constant peak RF (RFp) and negative RF relative to the peak RF (RFn; Fig. 1). After the RF peak, Tp is due to the slow warming Tp_s, while the RFn scenario produces both fast and slow cooling components (Tn_f and Tn_s). The ratios between these components jointly shape the evolution of GMST in RCP2.6 (Figs. 4 and 5). In particular, the slow warming component from the RFp scenario causes 0.2°C GMST rise by 2100, which is a sizeable magnitude compared to the 1.5°–2°C warming target given that current level of GMST rise has exceeded 1°C (Arndt et al. 2017; Xie and Kosaka 2017). Furthermore, surface temperature change referenced to the RF peak displays nearly flat cooling structure in the tropics but enhanced warming in the Southern Ocean, southern subtropics, and North Atlantic Ocean despite decreased GMST (Figs. 7c,d), due to the great offset between the decomposed warming pattern and cooling pattern (Figs. 7e–l). The slow deep ocean warming also directly fuels the persistent global-mean sea level rise due to thermal expansion of seawater (Fig. 5).

We show that in the low warming target where an RF increase is followed by a decrease, the percentage contribution to GMST rise from the ocean slow response increases with time. Specifically, the percentage contribution of the slow warming component to total GMST rise (referenced to preindustrial level) increases from around 10% during 2080–2100 to around 40% during 2280–2300 (Fig. 5; red line), compensating the effect of decreasing RF (Fig. 5; blue and green lines). The surface cooling pattern during decreasing RF period resembles the surface warming pattern during increasing RF period with the opposite sign (Figs. 7a,e–g). Given that previous climate change studies mostly focused on results from high emission scenarios where RF increases in time, in-depth investigations that quantify contributions from slow ocean processes to the surface pattern are required under a low warming scenario.

GMST is a convenient index tracking the anthropogenic climate change but its effectiveness suffers from the interference by internal variability as in the early 2000s global warming hiatus (Xie and Kosaka 2017). Global OHC has been increasing steadily (Fig. 5) and is suggested to be a more robust metric that tracks climate change. In RCP2.6, trends in RF and the radiatively forced GMST change turn negative in the mid-twenty-first century but OHC continues to increase and thus fails as an index tracking surface climate change. After the RF peak, the OHC change pattern mainly follows the distribution of the deep ocean warming, a result of the accumulated surface heat uptake and heat redistribution due to ocean heat transport.

The fast upper-ocean adjustment and slow deep ocean evolution are robust across climate models and regions (Fig. 11), but the deep ocean warming diverges in magnitude and penetration depth across basins. It is most pronounced and penetrates to great depths in the Atlantic Ocean but is relatively weak and shallow in the Indo-Pacific Ocean, a result of the interbasin differences in ocean dynamics, especially MOC. In the Southern Ocean, the subsurface warming can reach the bottom layer south of 50°S. The strong surface heat absorption around 60°S is transported northward by climatology Ekman flow, then pumped downward around 45°S and redistributed within the Deacon cell, leading to pronounced ocean warming north of 50°S. The effect of the AMOC on the Atlantic deep ocean warming involves processes associated with both AMOC weakening and mean AMOC. The weakened AMOC leads to significant heat uptake north of 30°N in the Atlantic due to a larger cooling in SST than surface air (Figs. 9 and 10). This heating further increases the subsurface ocean warming magnitude and increases (reduces) the penetration depth of warming south (north) of 30°N (Xie and Vallis 2012; Garuba and Klinger 2016). In RCP2.6, the air–sea contrast in surface temperature change over the North Atlantic weakens in response to RF decrease but remains positive through 2300. This is mainly because the AMOC stays in the weakened state despite its gradual recovery, allowing reduced but persistent OHU over the North Atlantic Ocean. The mean AMOC, on the other hand, transports the anthropogenic heat into the deep layer and throughout the Atlantic Ocean and to other basins (Garuba and Klinger 2016). The intermodel differences in AMOC weakening is tightly associated with the intensity of mean AMOC, with models of stronger mean AMOC showing a larger AMOC response to RF change. The deep ocean slow warming can further trigger coupled ocean–atmosphere adjustments by indirect feedback on surface climate change and further cause regional climate change (Xie et al. 2010; Luo et al. 2017). Therefore, it is important to improve climate models in reproducing the mean circulation to capture ocean slow response and achieve reliable surface climate projections.

Acknowledgments. We acknowledge the WCRP Working Group on Coupled Modeling, which is responsible for CMIP, and the climate modeling groups for producing and making available their model outputs. All data were downloaded from http://pcmdi9.llnl.gov/. This work is supported by the Natural Science Foundation of China (NSFC; 41706026, 41831175, 41525019, 41830538), "the Fundamental Research Funds for the Central Universities" (2018B04814, 2017B20714), the open fund of State Key Laboratory of Satellite Ocean Environment Dynamics, Second Institute of Oceanography (QNHX1808), National Key Research and Development Program of China (2016YFA0601804, 2018YFA0605702), the National Basic Research Program of China (2012CB955600), the NSFC-Shandong Joint Fund for Marine Science Research Centers (U1406401), the Priority Academic Program Development of Jiangsu Higher Education Institutions (PAPD), and Key Special Project for Introduced Talents Team of Southern Marine Science and Engineering Guangdong Laboratory (Guangzhou) (GML2019ZD0303).

REFERENCES

Bitz, C. M., P. R. Gent, R. A. Woodgate, M. M. Holland, and R. Lindsay, 2006: The influence of sea ice on ocean heat uptake in response to increasing CO_2. *J. Climate*, **19**, 2437–2450, https://doi.org/10.1175/JCLI3756.1.

Blunden, J., and D. S. Arndt, Eds., 2017: State of the Climate in 2016. *Bull. Amer. Meteor. Soc.*, **98** (8), S1–S277, https://doi.org/10.1175/2017BAMSStateoftheClimate.1.

Chadwick, R., P. L. Wu, P. Good, and T. Andrews, 2013: Asymmetries in tropical rainfall and circulation patterns in idealised CO_2 removal experiments. *Climate Dyn.*, **40**, 295–316, https://doi.org/10.1007/s00382-012-1287-2.

Chen, C., W. Liu, and G. Wang, 2019: Understanding the uncertainty in the 21st century dynamic sea level projections: The role of the AMOC. *Geophys. Res. Lett.*, **46**, 210–217, https://doi.org/10.1029/2018GL080676.

Cheng, L., J. Abraham, Z. Hausfather, and K. E. Trenberth, 2019: How fast are the oceans warming? *Science*, **363**, 128–129, https://doi.org/10.1126/science.aav7619.

Church, J. A., and N. J. White, 2011: Sea-level rise from the late 19th to the early 21st century. *Surv. Geophys.*, **32**, 585–602, https://doi.org/10.1007/s10712-011-9119-1.

Frölicher, T. L., M. Winton, and J. L. Sarmiento, 2014: Continued global warming after CO_2 emissions stoppage. *Nat. Climate Change*, **4**, 40–44, https://doi.org/10.1038/nclimate2060.

Garuba, O. A., and B. A. Klinger, 2016: Ocean heat uptake and interbasin transport of the passive and redistributive components of surface heating. *J. Climate*, **29**, 7507–7527, https://doi.org/10.1175/JCLI-D-16-0138.1.

——, and ——, 2018: The role of individual surface flux components in the passive and active ocean heat uptake. *J. Climate*, **31**, 6157–6173, https://doi.org/10.1175/JCLI-D-17-0452.1.

Geoffroy, O., D. Saint-Martin, D. J. L. Olivié, A. Voldoire, G. Bellon, and S. Tytéca, 2013a: Transient climate response in a two-layer energy-balance model. Part I: Analytical solution and parameter calibration using CMIP5 AOGCM experiments. *J. Climate*, **26**, 1841–1857, https://doi.org/10.1175/JCLI-D-12-00195.1.

——, ——, ——, ——, ——, and ——, 2013b: Transient climate response in a two-layer energy-balance model. Part II: Representation of the efficacy of deep-ocean heat uptake and validation for CMIP5 AOGCMs. *J. Climate*, **26**, 1859–1876, https://doi.org/10.1175/JCLI-D-12-00196.1.

Gregory, J. M., 2000: Vertical heat transports in the ocean and their effect on time-dependent climate change. *Climate Dyn.*, **16**, 501–515, https://doi.org/10.1007/s003820000059.

——, and R. Tailleux, 2011: Kinetic energy analysis of the response of the Atlantic meridional overturning circulation to CO_2-forced climate change. *Climate Dyn.*, **37**, 893–914, https://doi.org/10.1007/s00382-010-0847-6.

——, and Coauthors, 2005: A model intercomparison of changes in the Atlantic thermohaline circulation in response to increasing atmospheric CO_2 concentration. *Geophys. Res. Lett.*, **32**, L12703, https://doi.org/10.1029/2005GL023209.

——, and Coauthors, 2016: The Flux-Anomaly-Forced Model Intercomparison Project (FAFMIP) contribution to CMIP6: Investigation of sea-level and ocean climate change in response to CO_2 forcing. *Geosci. Model Dev.*, **9**, 3993–4017, https://doi.org/10.5194/gmd-9-3993-2016.

Haskins, R. K., K. I. C. Oliver, L. C. Jackson, S. S. Drijfhout, and R. A. Wood, 2019: Explaining asymmetry between weakening and recovery of the AMOC in a coupled climate model. *Climate Dyn.*, **53**, 67–79, https://doi.org/10.1007/s00382-018-4570-z.

Held, I. M., M. Winton, K. Takahashi, T. Delworth, F. R. Zeng, and G. K. Vallis, 2010: Probing the fast and slow components of global warming by returning abruptly to preindustrial forcing. *J. Climate*, **23**, 2418–2427, https://doi.org/10.1175/2009JCLI3466.1.

IPCC, 2013: *Climate Change 2013: The Physical Science Basis*. T. F. Stocker et al., Eds., Cambridge University Press, 1535 pp.

——, 2018: Summary for policymakers. Global warming of 1.5°C: An IPCC Special Report on the impacts of global warming of 1.5°C above pre-industrial levels and related global greenhouse gas emission pathways, in the context of strengthening the global response to the threat of climate change, sustainable development, and efforts to eradicate poverty. V. Masson-Delmotte et al., Eds., World Meteorological Organization, 1–24, https://www.ipcc.ch/sr15/.

Kim, H., and S.-I. An, 2013: On the subarctic North Atlantic cooling due to global warming. *Theor. Appl. Climatol.*, **114**, 9–19, https://doi.org/10.1007/s00704-012-0805-9.

Levitus, S., and Coauthors, 2012: World ocean heat content and thermosteric sea level change (0–2000 m), 1955–2010. *Geophys. Res. Lett.*, **39**, L10603, https://doi.org/10.1029/2012GL051106.

Li, D., T. Zhou, L. Zou, W. Zhang, and L. Zhang, 2018: Extreme high-temperature events over East Asia in 1.5°C and 2°C warmer futures: Analysis of NCAR CESM low-warming experiments. *Geophys. Res. Lett.*, **45**, 1541–1550, https://doi.org/10.1002/2017GL076753.

Liu, W., and A. Fedorov, 2019: Global impacts of Arctic sea ice loss mediated by the Atlantic meridional overturning circulation. *Geophys. Res. Lett.*, **46**, 944–952, https://doi.org/10.1029/2018GL080602.

——, S.-P. Xie, and J. Lu, 2016: Tracking ocean heat uptake during the surface warming hiatus. *Nat. Commun.*, **7**, 10926, https://doi.org/10.1038/ncomms10926.

——, ——, Z. Liu, and J. Zhu, 2017: Overlooked possibility of a collapsed Atlantic meridional overturning circulation in

warming climate. *Sci. Adv.*, **3**, e1601666, https://doi.org/10.1126/sciadv.1601666.

——, J. Lu, S.-P. Xie, and A. V. Fedorov, 2018: Southern Ocean heat uptake, redistribution and storage in a warming climate: The role of meridional overturning circulation. *J. Climate*, **31**, 4727–4743, https://doi.org/10.1175/JCLI-D-17-0761.1.

——, A. Fedorov, and F. Sévellec, 2019: The mechanisms of the Atlantic meridional overturning circulation slowdown induced by Arctic sea ice decline. *J. Climate*, **32**, 977–996, https://doi.org/10.1175/JCLI-D-18-0231.1.

Long, S.-M., S.-P. Xie, X.-T. Zheng, and Q. Liu, 2014: Fast and slow responses to global warming: Sea surface temperature and precipitation patterns. *J. Climate*, **27**, 285–299, https://doi.org/10.1175/JCLI-D-13-00297.1.

——, ——, and W. Liu, 2016: Uncertainty in tropical rainfall projections: Atmospheric circulation effect and the ocean coupling. *J. Climate*, **29**, 2671–2687, https://doi.org/10.1175/JCLI-D-15-0601.1.

——, ——, Q. Liu, X. Zheng, G. Huang, K. Hu, and Y. Du, 2018: Slow ocean response and the 1.5° and 2°C warming targets (in Chinese). *Chin. Sci. Bull.*, **63**, 558–570, https://doi.org/10.1360/N972017-01115.

Luo, Y., J. Lu, F. Liu, and O. Garuba, 2017: The role of ocean dynamical thermostat in delaying the El Niño–like response over the equatorial Pacific to climate warming. *J. Climate*, **30**, 2811–2827, https://doi.org/10.1175/JCLI-D-16-0454.1.

Manabe, S., and R. Stouffer, 2007: Role of ocean in global warming. *J. Meteor. Soc. Japan*, **85B**, 385–403, https://doi.org/10.2151/jmsj.85B.385.

——, K. Bryan, and M. J. Spelman, 1990: Transient response of a global ocean–atmosphere model to a doubling of atmospheric carbon dioxide. *J. Phys. Oceanogr.*, **20**, 722–749, https://doi.org/10.1175/1520-0485(1990)020<0722:TROAGO>2.0.CO;2.

Mann, M. E., 2009: Defining dangerous anthropogenic interference. *Proc. Natl. Acad. Sci. USA*, **106**, 4065–4066, https://doi.org/10.1073/pnas.0901303106.

Marshall, D. P., and L. Zanna, 2014: A conceptual model of ocean heat uptake under climate change. *J. Climate*, **27**, 8444–8465, https://doi.org/10.1175/JCLI-D-13-00344.1.

Marshall, J. K., J. R. Scott, K. C. Armour, J.-M. Campin, M. Kelley, and A. Romanou, 2015: The ocean's role in the transient response of climate to abrupt greenhouse gas forcing. *Climate Dyn.*, **44**, 2287–2299, https://doi.org/10.1007/s00382-014-2308-0.

Morrison, A. K., S. M. Griffies, M. Winton, W. G. Anderson, and J. L. Sarmiento, 2016: Mechanisms of Southern Ocean heat uptake and transport in a global eddying climate model. *J. Climate*, **29**, 2059–2075, https://doi.org/10.1175/JCLI-D-15-0579.1.

Palter, J. B., T. L. Frölicher, D. Paynter, and J. G. John, 2018: Climate, ocean circulation, and sea level changes under stabilization and overshoot pathways to 1.5 K warming. *Earth Syst. Dyn.*, **9**, 817–828, https://doi.org/10.5194/esd-9-817-2018.

Rhein, M., and Coauthors, 2013: Observations: Ocean. *Climate Change 2013: The Physical Science Basis*, T. F. Stocker et al. Eds., Cambridge University Press, 255–316.

Rogelj, J., D. L. McCollum, B. C. O'Neill, and K. Riahi, 2013: 2020 emissions levels required to limit warming to below 2°C. *Nat. Climate Change*, **3**, 405–412, https://doi.org/10.1038/nclimate1758.

Rugenstein, M. A. A., M. Winton, R. J. Stouffer, S. M. Griffies, and R. Hallberg, 2013: Northern high-latitude heat budget decomposition and transient warming. *J. Climate*, **26**, 609–621, https://doi.org/10.1175/JCLI-D-11-00695.1.

Russell, G. L., and D. Rind, 1999: Response to CO_2 transient increase in the GISS Coupled Model: Regional coolings in a warming climate. *J. Climate*, **12**, 531–539, https://doi.org/10.1175/1520-0442(1999)012<0531:RTCTII>2.0.CO;2.

Sanderson, B. M., B. C. O'Neill, and C. Tebaldi, 2016: What would it take to achieve the Paris temperature targets? *Geophys. Res. Lett.*, **43**, 7133–7142, https://doi.org/10.1002/2016GL069563.

——, and Coauthors, 2017: Community climate simulations to assess avoided impacts in 1.5° and 2°C futures. *Earth Syst. Dyn.*, **8**, 827–847, https://doi.org/10.5194/esd-8-827-2017.

Schaeffer, M., W. Hare, S. Rahmstorf, and M. Vermeer, 2012: Long-term sea-level rise implied by 1.5°C and 2°C warming levels. *Nat. Climate Change*, **2**, 867–870, https://doi.org/10.1038/nclimate1584.

Schleussner, C. F., P. Pfleiderer, and E. M. Fischer, 2017: In the observational record half a degree matters. *Nat. Climate Change*, **7**, 460–462, https://doi.org/10.1038/nclimate3320.

Sévellec, F., A. V. Fedorov, and W. Liu, 2017: Arctic sea-ice decline weakens the Atlantic meridional overturning circulation. *Nat. Climate Change*, **7**, 604–610, https://doi.org/10.1038/nclimate3353.

Sgubin, G., D. Swingedouw, S. Drijfhout, Y. Mary, and A. Bennabi, 2017: Abrupt cooling over the North Atlantic in modern climate models. *Nat. Commun.*, **8**, 14375, https://doi.org/10.1038/ncomms14375.

Shi, J., S.-P. Xie, and L. D. Tally, 2018: Evolving relative importance of the Southern Ocean and North Atlantic in anthropogenic ocean heat uptake. *J. Climate*, **31**, 7459–7479, https://doi.org/10.1175/JCLI-D-18-0170.1.

Taylor, K. E., R. J. Stouffer, and G. A. Meehl, 2012: An overview of CMIP5 and the experiment design. *Bull. Amer. Meteor. Soc.*, **93**, 485–498, https://doi.org/10.1175/BAMS-D-11-00094.1.

Trenberth, K. E., J. T. Fasullo, and M. A. Balmaseda, 2014: Earth's energy imbalance. *J. Climate*, **27**, 3129–3144, https://doi.org/10.1175/JCLI-D-13-00294.1.

van Vuuren, D. P., and Coauthors, 2011: The representative concentration pathways: An overview. *Climatic Change*, **109**, 5–31, https://doi.org/10.1007/s10584-011-0148-z.

Weaver, A. J., M. Eby, M. Kienast, and O. A. Saenko, 2007: Response of the Atlantic meridional overturning circulation to increasing atmospheric CO_2: Sensitivity to mean climate state. *Geophys. Res. Lett.*, **34**, L05708, https://doi.org/10.1029/2006GL028756.

Wen, Q., J. Yao, K. Döös, and H. Yang, 2018: Decoding hosing and heating effects on global temperature and meridional circulations in a warming climate. *J. Climate*, **31**, 9605–9623, https://doi.org/10.1175/JCLI-D-18-0297.1.

Williams, K. D., W. J. Ingram, and J. M. Gregory, 2008: Time variation of effective climate sensitivity in GCMs. *J. Climate*, **21**, 5076–5090, https://doi.org/10.1175/2008JCLI2371.1.

Winton, M., K. Takahashi, and I. M. Held, 2010: Importance of ocean heat uptake efficacy to transient climate change. *J. Climate*, **23**, 2333–2344, https://doi.org/10.1175/2009JCLI3139.1.

——, S. M. Griffies, B. L. Samuels, J. L. Sarmiento, and T. L. Frölicher, 2013: Connecting changing ocean circulation with changing climate. *J. Climate*, **26**, 2268–2278, https://doi.org/10.1175/JCLI-D-12-00296.1.

Xie, P., and G. K. Vallis, 2012: The passive and active nature of ocean heat uptake in idealized climate change experiments. *Climate Dyn.*, **38**, 667–684, https://doi.org/10.1007/s00382-011-1063-8.

Xie, S.-P., and Y. Kosaka, 2017: What caused the global surface warming hiatus of 1998–2013? *Curr. Climate Change Rep.*, **3**, 128–140, https://doi.org/10.1007/s40641-017-0063-0.

——, C. Deser, G. A. Vecchi, J. Ma, H. Teng, and A. T. Wittenberg, 2010: Global warming pattern formation: Sea surface temperature and rainfall. *J. Climate*, **23**, 966–986, https://doi.org/10.1175/2009JCLI3329.1.

——, B. Lu, and B. Xiang, 2013: Similar spatial patterns of climate responses to aerosol and greenhouse gas changes. *Nat. Geosci.*, **6**, 828–832, https://doi.org/10.1038/ngeo1931.

——, and Coauthors, 2015: Towards predictive understanding of regional climate change. *Nat. Climate Change*, **5**, 921–930, https://doi.org/10.1038/nclimate2689.

Xu, Y., and V. Ramanathan, 2017: Well below 2°C: Mitigation strategies for avoiding dangerous to catastrophic climate changes. *Proc. Natl. Acad. Sci. USA*, **114**, 10 315–10 323, https://doi.org/10.1073/pnas.1618481114.

Zheng, X.-T., C. Hui, S.-P. Xie, W. Cai, and S.-M. Long, 2019: Intensification of El Niño rainfall variability over the tropical Pacific in the slow oceanic response to global warming. *Geophys. Res. Lett.*, **46**, 2253–2260, https://doi.org/10.1029/2018GL081414.

Zickfeld, K., S. Solomon, and D. M. Gilford, 2017: Centuries of thermal sea-level rise due to anthropogenic emissions of short-lived greenhouse gases. *Proc. Natl. Acad. Sci. USA*, **114**, 657–662, https://doi.org/10.1073/pnas.1612066114.